scientific reports

Check for updates

OPEN

# Biocompatibility and bone regeneration with elastin-like recombinamer-based catalyst-free click gels

I. N. Camal Ruggieri[1]✉, M. Aimone[1], D. Juanes-Gusano[4], A. Ibáñez-Fonseca[4], O. Santiago[1], M. Stur[1,7], J. P. Mardegan Issa[2], L. R. Missana[5,6], M. Alonso[4]✉, J. C. Rodríguez-Cabello[4] & S. Feldman[1,3]✉

**Large bone defects are a significant health problem today with various origins, including extensive trauma, tumours, or congenital musculoskeletal disorders. Tissue engineering, and in particular bone tissue engineering, aims to respond to this demand. As such, we propose a specific model based on Elastin-Like Recombinamers-based click-chemistry hydrogels given their high biocompatibility and their potent on bone regeneration effect conferred by different bioactive sequences. In this work we demonstrate, using biochemistry, histology, histomorphometry and imaging techniques, the biocompatibility of our matrix and its potent effect on bone regeneration in a model of bone parietal lesion in female New Zealand rabbits.**

**Keywords** Scaffold, Elastin, Bone, Tissue engineering

Bone tissue contains a variety of cells, including osteocytes, osteoblasts, and osteoclasts, which are embedded in an extracellular matrix (ECM) composed of water, collagen fibres, and crystallized mineral salts such as hydroxyapatite, which provides strength and flexibility to the bone tissue[1]. In addition to facilitating locomotion, bone tissue serves to support and protect vital organs, stores calcium and phosphate, and the harbouring of bone marrow for blood cell production[2].

Extensive trauma, tumours, or congenital musculoskeletal disorders, impacting healthcare and the economy[3–7]. Tissue engineering employs scaffolds to regenerate tissues, addressing challenges like tissue morbidity and poor vascularization[8–10]. Bone tissue engineering focuses on active scaffolds with biocompatibility, mechanical properties, and biodegradability to facilitate new bone tissue growth[11].

Natural polymers, such as chitosan, collagen, hyaluronic acid, fibroin and gelatine, offer excellent biocompatibility and biodegradability, which facilitate bone tissue growth. However, their weak mechanical properties and rapid degradation limit their use in bone regeneration[12–17]. Synthetic polymers, such as polylactic acid (PLA), polycaprolactone (PCL), and poly (lactic-co-glycolic acid) (PLGA), offer superior mechanical strength but exhibit poor biocompatibility, which may result in the development of inflammatory responses and reduced cell adhesion[18–20]. Given the limitations that many biomaterials for bone tissue regeneration, complex materials are being developed, including composite materials with micro- and nanoscale morphologies that often combine bioceramics (HAP, MgO, etc.) and polymers materials[21]. In some cases, these composites include growth factors such as BMP2 or BMP7, which regulate cell proliferation, differentiation, and extracellular matrix generation[22]. Nevertheless, the challenge of optimizing the binding efficiency of seeded cells to these scaffolds and improving clinical outcomes remains.

[1]LABOATEM. Osteoarticular Biology, Tissue Engineering and Emerging Therapies Laboratory, School of Medicine, National Rosario University, Rosario, Argentina. [2]Ribeirão Preto School of Dentistry, São Paulo University, São Paulo, Brazil. [3]Research Council of the National Rosario University (CIUNR) and CONICET, Rosario, Argentina. [4]BIOFORGE Lab, University of Valladolid, CIBER-BBN, Valladolid, Spain. [5]Experimental Pathology and Tissue Engineering Laboratory, School of Dentistry, National Tucumán University, Tucumán, Argentina. [6]Tissues Laboratory, IMMCA-CONICET, Tucumán, Argentina. [7]Diagnostic Imaging and Radiology, School of Medicine, National Rosario University, Rosario, Argentina. ✉email: ivannadircamalruggieri@gmail.com; malonso@eii.uva.es; saryfeldman@gmail.com

An alternative strategy, which is currently under constant development, is tissue engineering based on recombinant proteins, thereby obtaining tailored proteins or protein combinations, such as "silk-collagen," "silk-laminin," and "elastin-resilin-collagen," which have been demonstrated the extensive design possibilities offered by genetic engineering[23–25]. These materials offer a number of clear advantages, including the possibility of large-scale production and the freedom from limitations imposed by natural sources[26]. Their composition can be tailored for specific applications, thereby ensuring well-defined, reproducible properties and various bioactivities that mimic the extracellular matrix (ECM)[27]. Furthermore, the mechanical properties can be modified according to the composition. Elastin-like recombinamers (ELRs) have demonstrated considerable potential in the field of regenerative medicine, particularly in the context of bone tissue regeneration[28].

Elastin is a structural protein found in connective tissue that confer elasticity and resilience to organs such as blood vessels, lungs, and skin. Some elastin-based peptides have been demonstrated to participate in cell signalling, including processes such as proliferation and angiogenesis. Due to the insolubility of natural elastin derived from animal sources, ELRs were developed using recombinant technology[29]. This allowed the incorporation of specific bioactive peptide sequences to enhance their functionality for bioengineering applications.

ELRs are synthetic polypeptides based on the L-Val-L-Pro-Gly-X-Gly (VPGXG) pentapeptide sequence, which closely resembles native tropoelastin and in which X (guest residue) can be any amino acid except L-proline. The self-assembly of these molecules occurs above a transition temperature (Tt) through hydrophobic interactions[30,31]. ELRs exhibit elasticity, thermal responsiveness, cytocompatibility, and low thrombogenicity, which are characteristics similar to those of natural elastin. In addition, the introduction of lysine residues in their side chain allows for the inclusion of azide and cyclooctyne groups for click chemistry without the need for a catalyst, resulting in a biocompatible, covalently cross-linked hydrogel with mechanical properties that closely resemble those of the ECM when mixed in solution[32].

In recent years, ELR-based click-chemistry hydrogels have shown promising results in tissue regeneration, including skeletal muscle, cardiac muscle, bone, and cartilage. These hydrogels combine biocompatibility[30] with injectability with cells, serving as both scaffold and drug-delivery system to promote tissue repair. For example, Pescador et al.[32] combined an RGD-cell adhesion-ELR bioactive polymer with human mesenchymal stromal cells (hMSCs) for hyaline cartilage regeneration. In another study, hMSCs were used with a proangiogenic ELR-based hydrogel containing endothelial cell-specific binding sequences (REDV) for hind-limb ischemia regeneration[33].

In addition to high biocompatibility, hydrogels used for tissue regeneration must be biodegradable within the body. Studies have utilized ELR-based hydrogels with biodegradation sequences to achieve this. Coletta et al.[28] developed a bone regeneration strategy using degradable and bioactive ELRs containing cell-adhesion (RGD) and osteoinductive BMP-2 domains, promoting slow BMP-2 release for lamellar bone formation. In a subsequent study, Ibánez-Fonseca et al.[33] utilized an ELR hydrogel to enhance skeletal muscle healing by promoting infiltration of pro-regenerative M2 macrophages, preventing fibrotic scar tissue. They developed non-crosslinked and covalently crosslinked hydrogels to fill volumetric muscle loss (VML) in rat tibialis anterior muscles successfully. Finally, Contessotto et al.[34] designed a novel hydrogel to modulate post-ischemic cardiac remodelling in non-transmural MI, sensitive to protease cleavage (MMP-2, MMP-9, MMP-13, and cathepsin K), effectively mimicking the ECM.

In our study, we selected two previously reported ELRs capable of forming chemical hydrogels using a click chemistry approach, incorporating biological signals for cell adhesion, proliferation, and metabolism. Both ELRs share the (VPGXG)n backbone but differ in bioactive sequences: HRGD6-azide with RGD domains for cell adhesion and HE5-cyclooctyne with MMPs and cathepsin k binding sites[34,35]. These stable scaffolds interact with surrounding cells when implanted and degrade over time via MMP action. Our hypothesis is that ELR-based hydrogel treatment in a parietal bone lesion promotes bone regeneration. An advantage of this approach is effective regeneration without needing to introduce cells alongside the biomaterial during therapy, simplifying practical and regulatory considerations.

## Materials and methods

### Ethical approval

The work was conducted following international regulations and ARRIVE guidelines (https://arriveguidelines.org). These regulations include well-established guidelines for animal care and handling to decrease pain and suffering of the animal, according to the 3Rs (replacement, reduction, and refinement). The project was accredited by the Bioethics Committee at the Faculty of Medical Sciences of the National University of Rosario under the code 80020220700113UR and Resolution NO. 4888/2022 for Bone and/or Cartilaginous Tissue Engineering III.

### Elastin-like recombinamers (ELRs)

*ELR biosynthesis and characterization*

Previous literature has extensively described the bioproduction of ELRs[29], and the polymers used in this work were designed, biosynthesized and provided by the BIOFORGE group at the University of Valladolid (Spain).

ELRs can be customized using genetic-engineering methods, thus allowing scalable production and consistent batch-to-batch outcomes. Briefly, the desired ELR sequence was genetically engineered in a double-strand DNA that contained the genes encoding for the elastin-like motifs in combination with cell-adhesion sequences and degradation domains, using the iterative recursive method. The resulting polypeptide was then expressed in E. coli (BLR (DE3)) and produced in a bioreactor. Afterwards, the polymer was easily purified using the inverse temperature transition in water[36]. This involved successive heating and cooling cycles followed by centrifugation. Once pure, the ELRs were dialyzed against ultra-pure water and sterile-filtered through 0.22 µm filters, prior to freeze-drying.

The ELRs were comprehensively characterized across different batches using various physicochemical techniques[37,38]. Transition temperature determination was carried out using differential scanning calorimetry (DSC). Molecular weight and purity assessment were performed using sodium dodecyl sulfate polyacrylamide gel electrophoresis (SDS-PAGE) and matrix-assisted laser desorption/ionization time-of-flight spectrometry (MALDI-TOF, Bruker Autoflex Speed MALDI-TOF, Bruker Corporation, USA). In addition, proton nuclear magnetic resonance spectroscopy (1H NMR, NMR 500, Agilent Technologies, USA) was used to obtain an ELR fingerprint, and HPLC to determine the amino acid composition.

This process allowed the production of the two ELRs used in this work, namely HRGD6 and HE5 (Fig. 1), both of which have been described previously[34,35,39]. The first component (HRGD6) contains the tripeptide of adhesion domains, L-Arg-Gly-L-Asp (RGD), found in natural fibronectin, which induces good adhesion features for most cell lines, mainly via αvβ3 and α5β1 integrins, in addition to elastin-like domains and crosslinking sites[40,41]. This polymer has a molecular weight of 60 kDa and the amino acid sequence is as follows:

MGSSHHHHHHSSGLVPRGSHMESLL[(VPGIG)2(VPGKG)(VPGIG)2]2AVTGRGDSPASS[(VPGIG)2(VPGKG)(VPGIG)2]2

The second component (HE5) includes multi-target protease-sensitive domains for biodegradation that are cleavable by MMP-2, MMP-9, MMP-13, and Cat K for biodegradation[42,43], in addition to elastin-like domains and crosslinking sites. This polymer has a molecular weight of 54 kDa and the amino acid sequence is as follows:

MGSSHHHHHHHHGLVPRGSHMG(KKK)2{[(VPGVG)4VPGEG]10(VGGGGGPMGPSGPWGGGGGVGGGGQPQGLAKGGGGGVGGGGGPQGIWGQGGGG)}2GGGGGKKKGGGGV

*ELR chemical modification*

Both HRGD6 and HE5 contain lysine-rich domains, which are susceptible to chemical modification via strain-promoted alkyne-azide cycloaddition (SPAAC) cross-linking within their structure[44]. Thus, HE5 was chemically modified at the ε-amine group present in the side chain of the lysine residues to introduce an activated cyclooctyne group. Similarly, HRGD6 underwent a similar reaction to introduce modification with an azide group. Subsequently, proton magnetic resonance was carried out in deuterated dimethyl sulfoxide (25 mg/ml, Sigma-Aldrich) to evaluate the modification rate of both polymers. The results showed a modification rate of 55–65% (from 14 to 16 modified lysines, out of 24) in HRGD6-N3 and 30–40% (3–4 modified lysines, out of 9) in HE5-C. These chemically modified ELRs were then used to obtain covalently crosslinked ELR hydrogels.

*ELR hydrogel preparation for in vitro and in vivo administration*

ELR-based hydrogel formation took place via the orthogonal SPAAC catalyst-free click reaction between HE5-C and HRGD6-N3 to give a stable hydrogel network combining biodegradation and cell-adhesion features[45].

For in vitro and in *vivo* testing, HRGD6-N3 and HE5-C were dissolved separately in sterile cold phosphate-buffered saline (PBS, pH 7.4) for 16–24 h. They were then mixed prior to injection in a 1:1.8 ratio, respectively, which was the optimal proportion to form stable hydrogels at 50 mg/mL, considering their difference in molecular weight and percentage chemical modification. The click chemistry reaction between the azide and cyclooctyne residues allows catalyst-free hydrogel formation. Cold sterile tips were used to carry out this procedure. The Eppendorf tube containing the ELR mixture (50 mg/ml) was incubated for 8 min in an ice bath (4 °C) for homogeneous initial crosslinking, then the mixture was pipetted into the injury site, where the hydrogel formation process was completed (body temperature, 37 °C).

A detail description of the physicochemical characterization of the HRGD6-HE5 hydrogel can be found in the study by Contessotto et al., especially in the supplementary information[34], where the transparency, rheological studies, microstructural morphology and swelling ratio are described, in addition to an in vitro protease-sensitivity assessment.

## In vitro *evaluation*

*Cell culture for viability assays*

Human foreskin fibroblasts (HFF-1; ATCC® SCRC-1041™, USA) were cultured in complete culture medium, i.e. DMEM 4.5 g/L glucose (Gibco, USA) supplemented with 15% foetal bovine serum (FBS; Gibco, USA) and 1% penicillin/streptomycin, at 37 °C and 10% CO2. All cells were used at passage 5–7 in subsequent experiments.

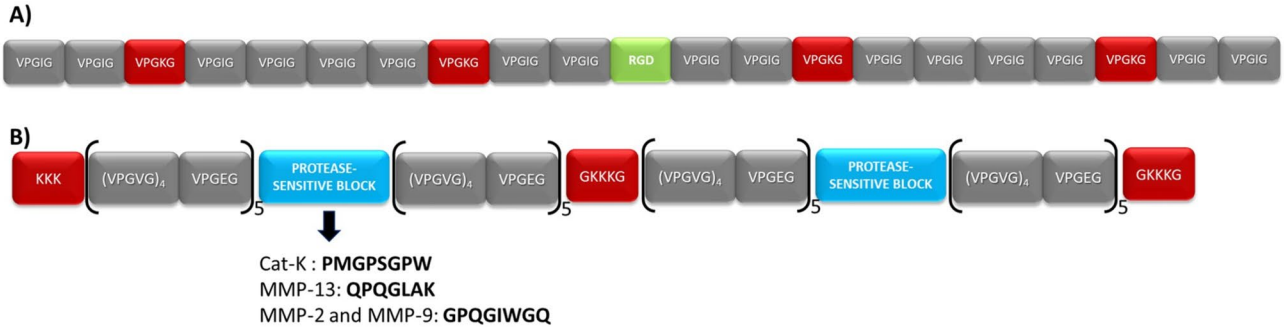


**Figure 1.** Graphical scheme of the ELR compositions: (**A**) HRGD6 and (**B**) HE5.

Cell encapsulation was attained by dissolving the ELRs as mentioned above, but using complete culture medium, and cells were added to the HRGD6-N3 solution. Both ELRs were then mixed, maintaining the 1:1.8 ratio and the 8-min incubation in an ice bath, and a 70 µL aliquot was deposited into the wells of a 96-well plate. The plate was placed at 37 °C, 10% $CO_2$ to complete hydrogel formation and, after 15 min, warm complete culture medium was added. The plates were cultured for 1 and 3 days and cells within the hydrogels were stained to determine cell viability and morphology. In the first case, hydrogels were directly stained with the LIVE/DEAD cell viability kit (Invitrogen, Thermo Fisher Scientific, USA) after 1 day of culture, following the manufacturer's instructions. To determine cell morphology, hydrogels were embedded after 1 and 3 days in a 4% (w/v) paraformaldehyde solution (Sigma-Aldrich, Merck KGaA, Germany) for 10 min for cell fixation, and subsequently in 0.1% (v/v) Triton X-100 (Sigma-Aldrich, Merck KGaA, Germany) for 5 min for cell permeabilization. Cells were then stained with a 1:40 dilution of Phalloidin-Alexa Fluor 488 (Invitrogen, Thermo Fisher Scientific, USA) for 30 min for actin staining, and nuclei were counterstained with a 300 nM DAPI (Invitrogen, Thermo Fisher Scientific, USA) solution for 2 min. All steps were performed at room temperature.

For image acquisition, hydrogels were placed on slides and observed with a fluorescence microscope (Nikon Eclipse Ti-E coupled to a Nikon DS-2MBWc digital camera; Nikon Corporation, Japan) at different magnifications. Z-stack videos were obtained using the NIS-Elements Advanced Research software (version 4.5; Nikon Corporation, Japan).

## In vivo *evaluation*

The animals subjected to bone damage and regeneration treatments were 12 female New Zealand white rabbits, 4-month-old with 3.5 kg average weight. Each animal stayed in an individual cage with ad libitum supply of food (Provife, Argentina) and water.

The animals subjected to bone damage and regeneration treatments were 12 female New Zealand white rabbits, 4-month-old with 3.5 kg average weight.

The animals were randomly assigned to two groups (n = 6 for each group). Group 1 was the control group, with no surgical intervention, and group 2 was intervened with two bone lesions in parietal bone: a left defect treated with ELR and a right defect as a control lesion. Before surgery, cefazolin (50 mg/kg/day) was administered intramuscularly as antibiotic prophylaxis and then they were anesthetized (35 mg/kg ketamine hydrochloride + 18 mg/kg xylazine hydrochloride 2%, + 1 mg/kg acepromazine maleate 1%). Before covering each rabbit's head with sterile fields, the areas were disinfected with 10% povidone-iodine solution. Skins incisions (5–6 cm in length) were parallel to the sagittal suture below the lambdoid sutures and the periosteums were dissected. A sterile electric drill was used for creating two 10 mm bone parietal lesion one on each side of the sagittal suture.

The mixing of solutions A and B was performed intraoperatively, and the chemical reaction was observed while it began. Once the solution had begun to gel, the hydrogel was placed inside the bone lesion in the left parietal bone using a sterile syringe. The matrix used finished gelling, due to the intrinsic thermal behavior properties of the ELRs, in contact with the animal (temperature approximately 36 °C). The periosteum was then sutured, covering the matrix without displacing it, with continuous stitches using resorbable thread. The skin was sutured and iodopovidone was passed over it. Post-surgical analgesia was provided with tramadol (100 mg/ml) 6 mg/kg/day IM. Prophylactic antibiotic treatment was continued for 5 days.

### *In vivo gelification*

While the hydrogel was placed inside the bone lesion in the left parietal bone, we observed the gelification process and checked that the hydrogel gels in a homogenous form with no unexpected outcomes.

### *Clinical control*

Every day during the first week and on days 15; 30 and 90, the following items were recorded: rectal temperature, water and food consumption, general condition and spontaneous mobility and signs of infection.

### *Biochemical studies*

Along the experiment, animal blood samples were extracted following conventional standard conditions and blood samples before sacrifice were used for hemogram data. All determinations were performed using Wiener lab Kits (Argentina). After samples homogenization, they were collected in EDTA tubes for red blood cells (RBC), white blood cells (WBC), haemoglobin (Hb), and platelets determination Samples without anticoagulant were used for serological hepatical transaminases (glutamate-oxalacetic transaminase, GOT and glutamate pyruvate transaminase, GPT), separating serum fraction by 10 min centrifugation at 10,000 rpm. All biochemical analysis was done at the onset of the experiment, one week after it and before animal euthanasia.

### *Animal euthanasia*

Second group animals were sedated (2% xylazine hydrochloride, plus an overdose of 2% sodium thiopental 1 g in 50 ml of double distilled water) and sacrificed 90 days after surgery following standards of the Bioethics Committee of Rosario National University (Resolution No 6838/2019).

### *Tomography studies*

All images were analysed together for an optimal comparison. Multislice computed tomography (MSCT) was performed on the heads of the rabbits using a Toshiba Alexion apparatus with 16 detectors and a thickness of 0.5 mm. Coronal, sagittal, and axial slices were obtained, and the images were processed using Alexion

Advance Edition software with the adaptive iterative dose reduction (AIDR 3D) algorithm, thus obtaining the 3D reconstruction for every sample.

*Histological studies*

The samples obtained were fixed in 10% buffered formalin for 24 h and dehydrated in ascending alcohol series as follows: 70%, 80%, 90% into ethanol (24 h) and 99% ethanol (72 h). Fixation and dehydration were carried out at room temperature (24 ± 5 °C). Four samples were decalcified by modified Morse solution (Okayama University Dental School) and embedded in paraffin following well-established protocols. After, they were serially cut (5 µm) to obtain oriented tissues, stained with H&E, Masson's Trichrome, and Verhoeff´s elastic stain. Two samples were embedded undecalcified into methyl methacrylate and stained using Masson-Goldner's Trichrome[46]. The first cuts from both technical procedures were stained previously by toluidine blue to allow us to be oriented into the tissues where control and experimental defects were performed. The defect´s size was determined using a millimetric grid into microscope's eyepiece and selected for staining.

All specimens were examined using a light microscope and evaluated by a single pathologist. After that, another pathologist (certified by the Health Ministry of Argentina. license N° 31,455) performed an independent review to verify microscopic observations. The reported results reflect the mutually agreed upon diagnoses by both pathologists. Photomicrographs were taken from slides of each specimen by means of an Olympus SC50 camera adapted to an Olympus BX 43 microscope using CellSens Standard 1.17 Olympus Soft 2009–2017 and Olympus stereo zoom SZ 51.

*Histomorphometric studies*

Microphotographs were taken from sections of each specimen, by an Olympus SC50 camera adapted to an Olympus BX 43 microscope using CellSens Standard 1.17 Olympus Soft 2009–2017. Photographs from each slide at bone critical defect (BCD) treated and not treated with the ELR matrix were obtained by 40X magnification. And the following compartments new bone, fibroblastic tissue or fibrous tissue, and new bone marrow were quantified. They were measured using the Image Pro Plus analysis system (Media Cybernetics, Silver Spring, MD, USA Version 4.5.0.29 for Windows 1998/NT/2000). Values were expressed as percentages[47,48]. An analysis of variance (ANOVA) was conducted for each variable of interest. Subsequently, to detect significant differences, the Tukey test was applied with a significance level of 0.05 (Montgomery, 2013). All assumptions were controlled to ensure confidence in the results.

*Statistical analysis*

Statistical analysis data for the in vitro experiments are reported as mean ± standard deviation. Statistical analysis of data following a normal distribution was performed using a one-way analysis of variance and the Holm–Sidak method. A p value of less than 0.05 was considered to be statistically significant, while $p > 0.05$ indicates no significant differences (n.s.d.). $^{*}p < 0.05$, $^{**}p < 0.01$. Statistical analysis of biochemical studies was performed with a non-parametric analysis of variance (Wilcoxon). A value of $p < 0.05$ was considered significant.

## Results

### In vitro evaluation

*LIVE/DEAD*

The evaluation of cell viability using the LIVE/DEAD assay showed that fibroblasts inside the hydrogel were viable. Figure 2a shows that cells were mostly alive (99%) within the ELR hydrogels after 1 day of culture, which reflects the high cytocompatibility of these hydrogels and of the SPAAC crosslinking method. This finding supports the potential use of the ELR hydrogels used in this work for tissue engineering and regenerative medicine applications, including bone tissue. The viability of the cells after culture for 3 days in media supplemented with the ELRs was found to be similar.

*Cell morphology*

Cells were also found to proliferate over time, as confirmed by the difference in the number and the shape of cells between day 1 and day 3. These time points were chosen to confirm that the hydrogel sample tested in this study was not cytotoxic; longer-term assays with the same hydrogel and cell line were conducted in previous studies[34].

As regards cell morphology, we found that cells were mostly rounded after only 1 day of culture, while they spread after 3 days, thus evidencing the role of RGD sequences that promote cell adhesion to the walls of the hydrogel. This result suggests that ELR hydrogels are able to mimic the extracellular matrix and that cells will be able to behave physiologically within the scaffolds (Fig. 2b).

### In vivo evaluation

*In vivo gelification*

The gelification process was observed during placement on all left parietal bone defects in homogeneous form, with no unexpected outcomes (Fig. 3).

*Clinical controls*

There were no significant differences between group 1 and group 2 in relation to rectal temperature, water and food consumption, general condition and spontaneous mobility during the period evaluated. In addition, there were no signs of infection on either the control side or the scaffold side.

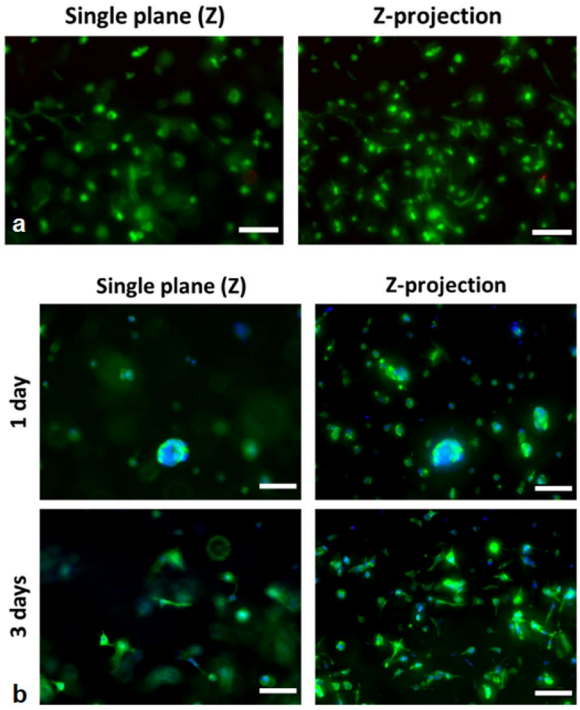


**Figure 2 (. a**) LIVE/DEAD images of HFF-1 cells within ELR hydrogels after 1 day of incubation. (**b**) A single plane of a field (left) and the Z-projection of a Z-stack of the same field (right) are shown. Green-stained cells correspond to living cells, while red dots are dead cells. Scale bar = 100 µm. b. Morphology of cells within ELR hydrogels stained with Phalloidin-Alexa Fluor 488 for actin staining (in green) and DAPI for nuclei (in blue). A single plane of a field (left) and the Z-projection of a Z-stack of the same field (right) are shown. Scale bar = 100 µm.

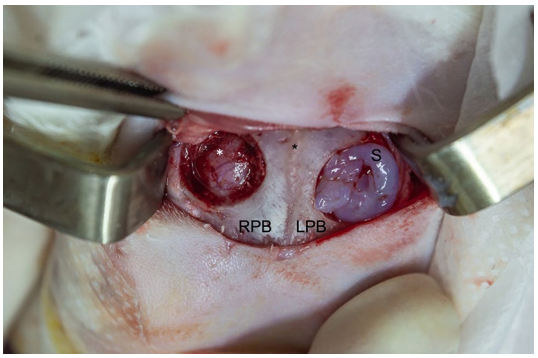


**Figure 3.** Intraoperative gelification. Skin incision on surgical calotte approach with a superior frontal view. The sagittal suture is in the middle (black asterisk), the 10 mm control defect with no scaffold is on the left-hand side (right parietal bone; RPB), and the 10 mm defect with scaffold is on the right-hand side (left parietal bone; LPB). The scaffold (S) starts to gelify within only 30 s since it is localized on the defect. The dura mater (white asterisk) and its vascularization can be seen on the left-hand side defect.

*Biochemical studies*

The results of the biochemistry studies at the beginning, at one week and at 90 days post-surgery did not show any statistically significant differences between the two groups. Figures 4 and 5 show hemograms and serum transaminases, respectively, at day 90. The biochemical statistical evaluation was performed using a non-parametric analysis of variance (Wilcoxon). A $p$ value of less than 0.05 was considered significant.

*Tomography studies*

A reduction in defect diameter on the implanted side in relation to the control side was observed in each experiment. No retraction of the surroundings tissue was observed on either side. A thin hyperdense sheet corresponding to total mineralization of the inner cortex of the parietal bone was observed on the implanted side.

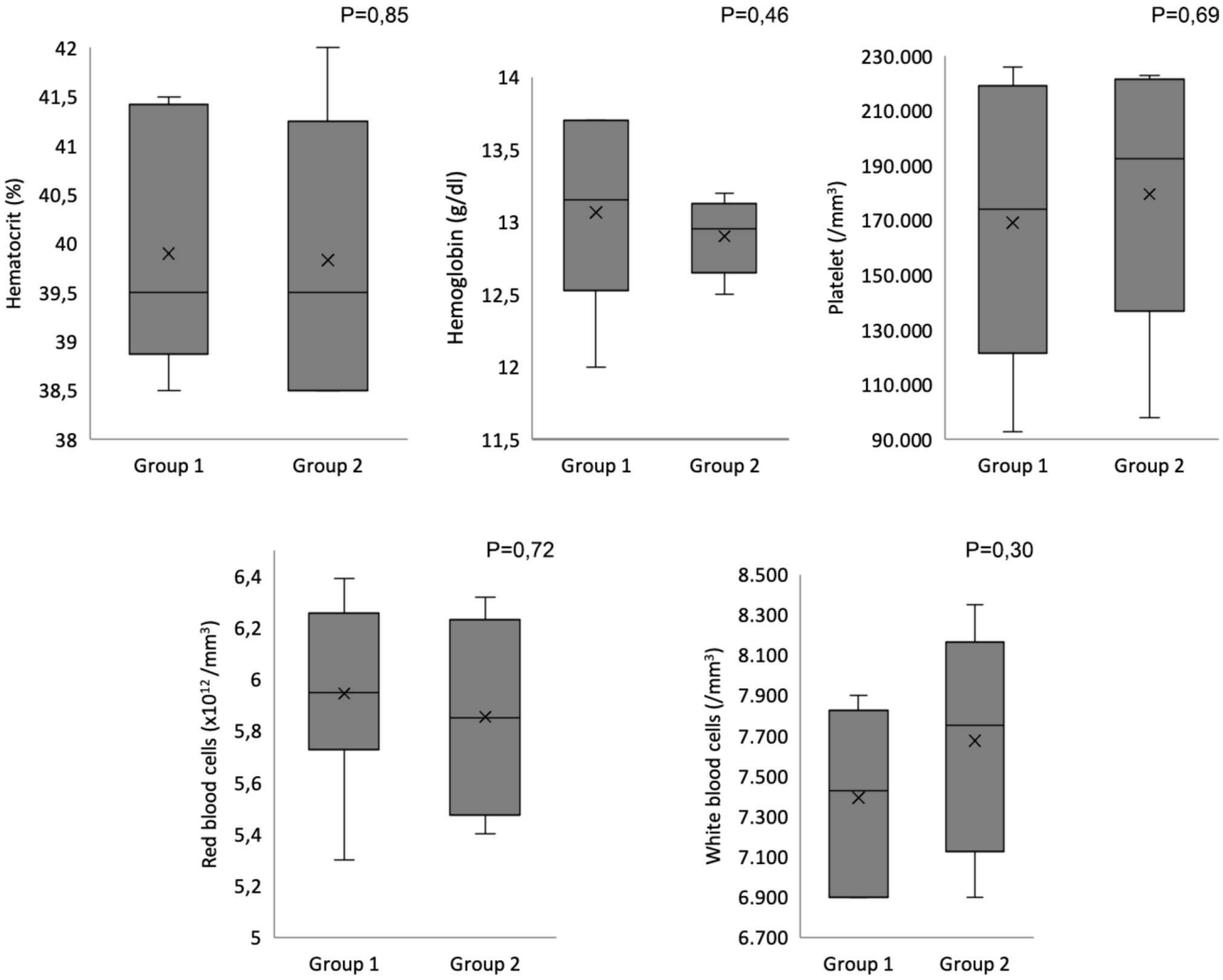


**Figure 4.** Hemogram results at 90 days in boxplot graphics.

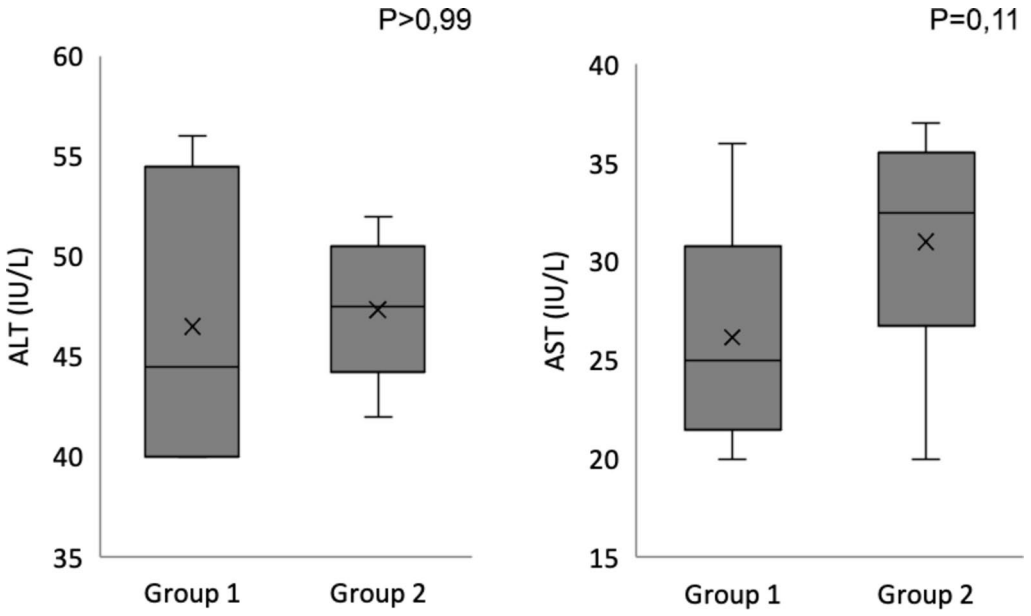


**Figure 5.** Serum transaminases result at 90 days in boxplot graphics.

Both the degree of diameter reduction of the defect (Fig. 6) and the type of tissue formed, which is confirmed by histological studies, have been very positive.

*Histological studies*

A. From Group 2, into the right side, slices showed (from top to bottom) skin, subcutaneous tissue, adipose tissue, muscle, and bone defect untreated area (BDUT) (Fig. 7a). The BDUT area was repaired with fibrous connective tissue, and a small amount of new bone was formed on each edge (Fig. 7a (left side), b).
B. From the left side, defect treated with ELR, shows (from top to bottom) skin, subcutaneous tissue, fibroblastic vascularized tissue, and the BDT (bone defect treated) area. The BDT area with ELRs showed new bone formation at edges and fibroblastic tissue. Many new vessels formation was observed very close to new bone formed (Fig. 8b,d,e). Moreover, some samples showed cells arranged in swirls within the fibroblastic tissue, with a similar appearance observed with normal intramembranous bone differentiation (Fig. 7b). Throughout the defect area, a series of multiple bone islets also co-called ossicles, were surrounded by fibroblastic tissue (Fig. 7d,e) This fibroblastic tissue will be reabsorbed as the islets grow in diameter, eventually combining to form a single bone structure. These islets were rounded, with hematopoietic bone marrow found in their core (Fig. 7c,d).
C. The new bone formed upon ELR stimulation shows a vascular space resembling Haver's system. Internally, it contains remnants of foreign material compatible with the ELRs and giant cells containing phagocytosed material. The flattened osteoblasts on the bone surface are known as inactive osteoblasts or lining-like cells. Osteoblast-like cells, with cuboidal cells, known as active osteoblasts, can also be seen (Fig. 8c). The new bone formed by the ELRs appears in various layers, showing a pagetoid-like pattern. Osteocytes were also observed distributed inside the newly formed bone. Bone tissue resting cells were also observed on the external surface (Fig. 7e), and remnants from the ELRs (Fig. 7e, 8a,b) inside the new bone formed in the BDA at the experimental group. The non-decalcified specimens showed thick osteoid layer formation between each new bone particle (Fig. 9a,b,c).

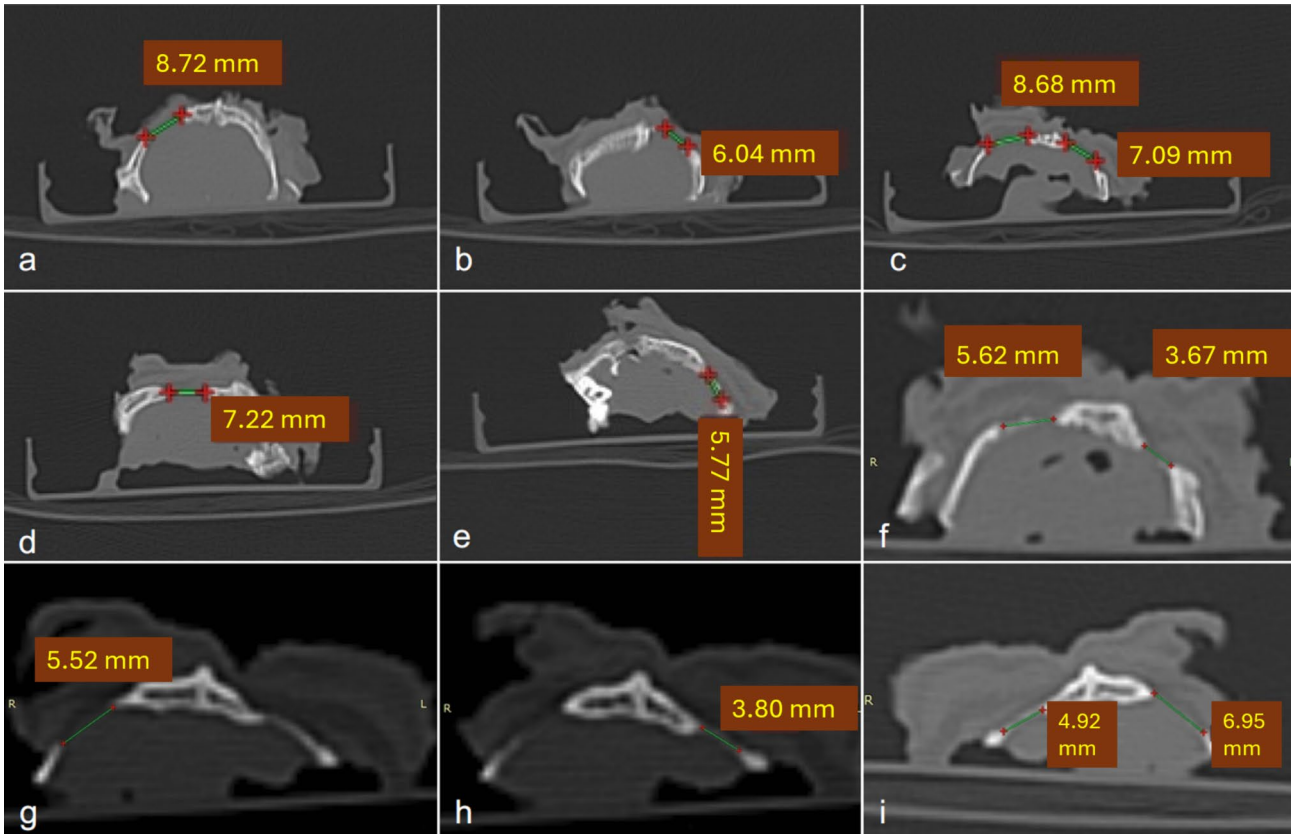


**Figure 6.** CT studies. (**a**) Diameter of the untreated right bone defect in rabbit 1. (**b**) Diameter of the left bone defect treated with ELRs in rabbit 1. (**c**) Diameter of the untreated right bone defect and diameter of left bone defect treated with ELRs in rabbit 2. (**d**) Diameter of the untreated right bone defect in rabbit 3. (**e**) Diameter of the left bone defect treated with ELRs in rabbit 3. (**f**) Diameter of the untreated right bone defect and diameter of the left bone defect treated with ELRs in rabbit 4. (**g**) Diameter of the untreated right bone defect in rabbit 5. (**h**) Diameter of the left bone defect treated with ELRs in rabbit 5. (**i**) Diameter of the untreated right bone defect and diameter of the left bone defect treated with ELRs in rabbit 6.

*Histomorphometric studies*

Based on microphotographs taken from sections of each specimen, a morphometric study was conducted, and the results can be observed in Fig. 10. Significant differences have been detected for Bone and Adipose Tissue/Others. In the case of Bone and considering the treatments performed, the following were obtained: Right side (29,2 ± 4,8%) and Left side with ELRs (68,2 ± 4,8%). On the other hand, for Adipose Tissue/Others the following were obtained: Right side (42,2 ± 6,4%) and Left side with ELRs (7,4 ± 6,4%).

## Discussion

The development of different hydrogels over the past few years has resulted in the availability of different alternatives for promoting the repair of damaged bone tissues[49]. In particular, herein we have developed and studied a hydrogel that possesses some very interesting characteristics for use in bone tissue engineering, namely: (A) it possesses a high biocompatibility, as seen at a clinical and biochemical level and by way of imaging and histological studies. The implantation process does not produce retraction of the surrounding host tissue, and no inflammatory cells were observed in the area around the implant or within the matrix. (B) The bone regeneration process was achieved without needing to include mesenchymal cells in the hydrogel. In this work we show that, at 90 days post-implantation of the hydrogel in a parietal bone lesion, directly at the site of the lesion, without any other type of aggregates, cell colonization occurs, the hydrogel was gradually degraded, and the cells are able to synthesize mineralized extracellular matrix, generating tissue compatible with newformed bone tissue. (C) The hydrogel promotes adequate neovascularization, which is essential for the bone-repair process. In certain cases, when a matrix is implanted to promote bone repair, insufficient vascularization may occur, thereby affecting tissue repair[50]. In this regard, although other groups have recently developed hydrogels that would, in principle, promote the necessary formations to achieve adequate vascularization a posteriori, the evidence presented is generally obtained in vitro[51,52]. Our in vivo results demonstrate that angiogenesis occurs, therefore we propose that the hydrogel must have promoted the proliferation, migration, and angiogenic differentiation of endothelial progenitor cells, thus generating adequate neovascularization, which allows the osteoblastic cells that colonize the hydrogel to be nourished, to synthesize extracellular matrix and, in some cases, to become osteocytes immersed in the mineralized matrix.

Considering the above, we can deduce the high efficacy of this hydrogel in the regeneration of bone defects. It is a simple system comprising two elastin-type biopolymers (HE5-C and HRGD6-$N_3$) that react with each other by means of a totally biocompatible "click chemistry" reaction. During the same therapeutic process, a covalently cross-linked hydrogel, which can be applied to the defect, in this case, the parietal bone (even by injection), following a simple process, is obtained in situ. In this way we generate a scaffold "tailored to the lesion" and which will not spread to the surrounding tissues, as often happens with natural biomaterials, due to the presence of the cross-link.

Despite having a higher consistency than its chemically non-crosslinked analogues, this scaffold exhibits very remarkable elastic properties comparable to those of different ECMs from different natural tissues as a result of its base composition, which simulates natural elastin[53].

As previously described, the hydrogel used in this study is formed through chemical cross-linking and contains two biofunctionalities: RGD domains for cell adhesion and MMP-sensitive domains for biodegradation. Regarding the first biofunctionality, the obtained results confirm that the RGD cell-adhesion sequence effectively recruits surrounding cells, facilitating the colonization of the hydrogel introduced into the bone lesion. It is noteworthy that the osteoinduction process has been effective without the need for additional osteoinductive bone morphogenetic proteins, such as BMP-2, as proposed in the work of Coletta et al.[28] for bone tissue regeneration using hydrogels also based on ELRs.

On the other hand, the histological results suggest that endothelial progenitor cells are present and can induce angiogenesis, facilitating the metabolism of the osteoblastic cells also embedded in the hydrogel. Moreover, these cells have been able to synthesize their own mineralized matrix with osteocytes embedded in it, without the need to include bioceramics in the scaffold.

The second biofunctionality of the hydrogel comprises multi-target protease-sensitive domains, such as MMP-2, MMP-9, MMP-13, and cathepsin K, which allow the simulation of a natural biodegradation process of the extracellular matrix. These metalloproteinase-sensitive domains were successfully tested both in skeletal muscle healing[33] and in the prevention of fibrotic tissue formation after myocardial infarction[34]. In the first case, recombinant silk-elastin-like polymers (SELRs) were used to form hydrogels through physical crosslinking and included MMP-sensitive and RGD domains. The presence of the MMP-sensitive sequences along with the RGD sequence promoted greater M2 macrophage infiltration at the injury site, leading to the formation of myofibers, reduced collagen deposition, and a muscle morphology more like healthy tissue compared to untreated controls. In the second case, a hydrogel obtained from ELRs through chemical crosslinking and containing MMP-sensitive, and RGD sequences demonstrated prevention of fibrosis formation and increased angiogenesis in the ischemic core region following the infarction. Complete functional remodeling of the ischemic core region was also observed, which then propagated its effect to the border region of the lesion, promoting its regeneration.

In the bone regeneration model studied in this work, similarly favorable results were observed, analogous to the previously mentioned studies. As the cells are introduced and proliferate within the hydrogel, they generate proteases that degrade the scaffold at the same rate as the new bone tissue appears. Thus, the hydrogel does not hinder the regeneration of the bone lesion and degrades as the cells produce their own natural extracellular matrix. Consequently, it has been demonstrated that with this ELR composition, the introduction of differentiation-inducing agents such as BMPs or bioceramics into the scaffold is not necessary. This hydrogel,

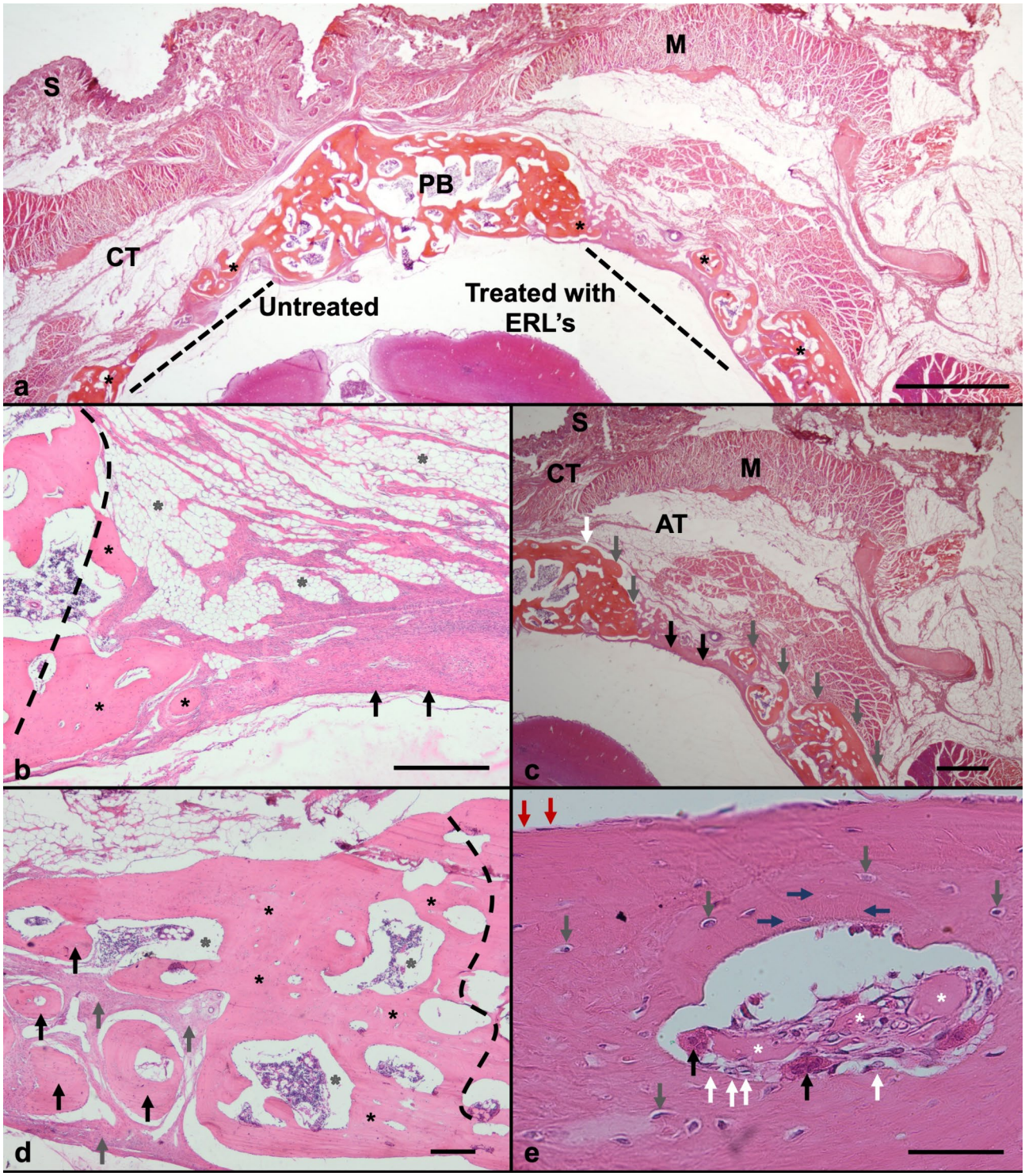
S
M
PB
CT
Untreated
Treated with
ERL's
a
b
S
CT
M
AT
c
d
e

◂**Figure 7.** Histological photography from decalcified samples and stained by H&E. (**a**) Panoramic image from bone defect area (BDA) on rabbit calvaria, it was showing (right) treated side by ELRs (BDT) and (left) untreated side (BDUT), at 90 days post-surgery. From top to bottom: skin (S), connective tissue (CT), muscle (M), parietal bone (PB), bone defect area (BDA), and brain. Bone formation (black asterisk) was observed on BD untreated and treated edges. The new bone inside BDT had similar thickness to normal bone. Also, multiple bone formations co-called ossicles were observed 6.3 X. Scale bar = 2 mm. (**b**) On BDUT area was trace (black dashed line) the defect edge, cover it by new bone formation (black asterisks). On its top shows fibro-adipose connective tissue (grey asterisks), under fibroblastic tissue arranged in swirling cells, over bone defect. This shows a biological mechanism to form new bone, in an intramembranous bone like differentiation process (black asterisks). 400X. Scale bar = 200 μm. (**c**) On BDT edge (white arrow) new bone (grey arrow) was found. Scarce fibroblastic tissue (black arrow) and new bone formations (grey arrows) covered BDT area. Also, hematopoietic bone marrow was seen inside ossicles. 6.3X. Scale bar = 2 mm. (**d**) At BDT, the edge traced (black dashed line) was covered by new bone (black asterisks) with hematopoietic bone marrow at their core (gray asterisks). Also, multiple rounded bone islets (black arrow), surrounded by fibroblastic tissue (grey arrow), were forming. The fibroblastic tissue will be replaced by bone islets grow in diameter until they merge to form a single bone structure. 40X. Scale bar = 200 μm. (**e**) Higher magnification, In BDT area new bone shows a Haver´s system-like, with ELRs remnants (white asterisks). These acts like foreign body material, with giant cells containing phagocytized material (black arrow). Osteoblast-like cells (white arrow) were seen on bone surface (endosteum). The bone appears in various layers. Osteocytes inside new bone (grey arrow) were connected by its cytoplasmic processes (blue arrow). Resting cells observed (red arrow) on bone tissue external surface (periosteum). 400x. Scale bar = 200 μm.

with its RGD adhesion sequences and metalloproteinase sensitivity, successfully recruits the necessary cells such as endothelial progenitor and osteoblastic cells. Also, the mesenchyme condenses into a rich vascularized connective tissue, with cells that contact to each other, and the intercellular space will be occupied by delicate collagen fibrils in a thin gel-like substance that generate first fibroblastic tissue and it will evolve to generate a viable mineralized bone matrix.

Finally, it is significant that the introduction of the hydrogel with embedded cells is not required to achieve a good regenerative process, offering benefits from both a therapeutic application and regulatory perspective.

In summary, the combination of the two functionalities, adhesion sequences and protease sensitivity, creates a synergistic tandem that promotes the recruitment and proliferation of cells from peripheral tissues and the proper spatiotemporal synchronization of their regenerative activity. Moreover, this is achieved without the need for other bioactive elements such as growth factors, inflammation controllers, or any other agents. This effect was already identified in the heart and muscle regeneration models, and now it is demonstrated in bone tissue.

## Conclusion

In summary, we have achieved excellent results by using a bicomponent hydrogel made exclusively of ELRs, under the premise that generating an optimal cellular environment is the most effective way for the cells surrounding the lesion to fully develop their regenerative capacity. Furthermore, the scaffold obtained has excellent biocompatibility since, although it is a recombinant biopolymer, its composition simulates natural proteins from the ECM. Moreover, this system is easy to apply in situ, there is no need to include a bioceramic phase, growth factors or other agents, and it will present less regulatory complexity since it does not include cells in the therapeutic process.

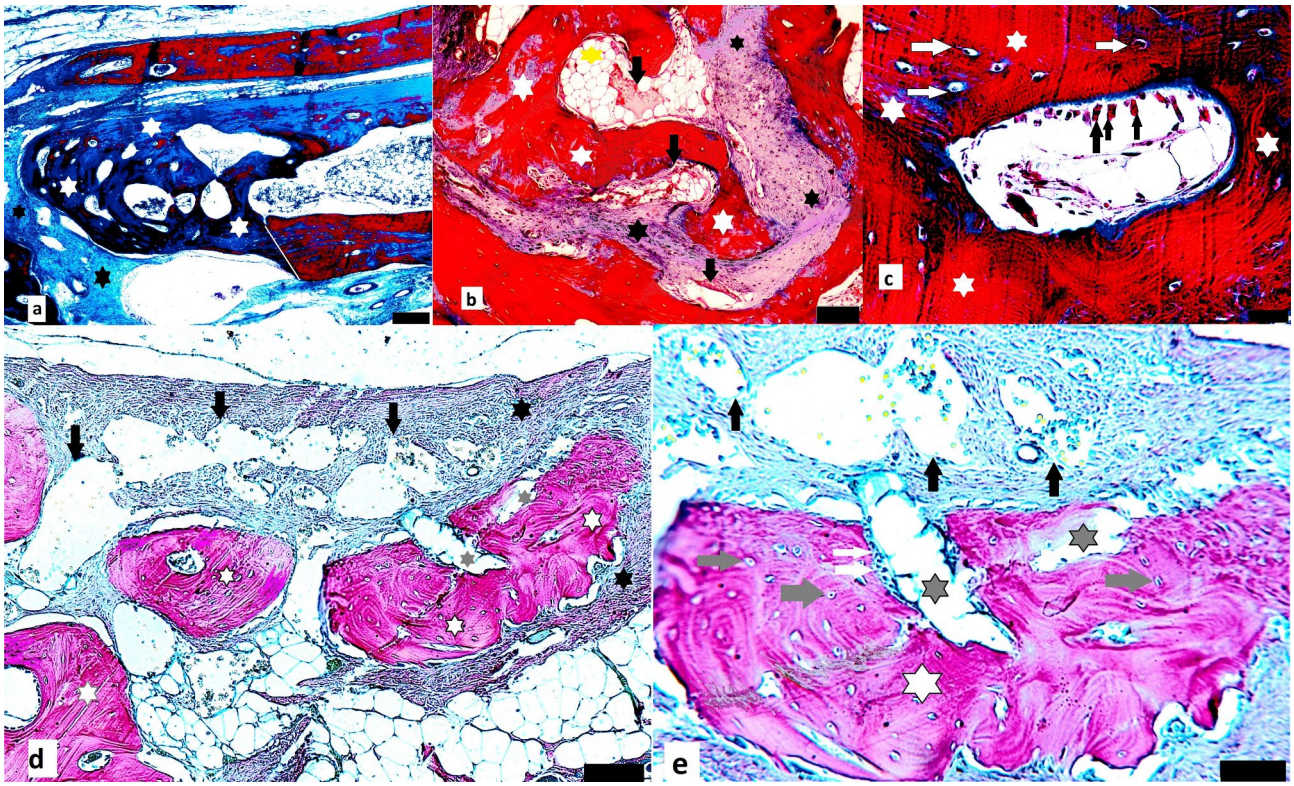


**Figure 8.** Histological photography from decalcified samples. (**a,b,c**) Stained by Masson's trichrome. (**a**) From BDT by ELRs after 90 days. It showed bone edge defect (white line) connected to newly formed bone (white asterisk) surrounded by fibroblastic tissue (black asterisk). Decalcified sample.40X. Scale bar 200 µm. (**b**) At BDT area shows inside fibroblastic tissue (black asterisk) a newly formed trabeculae (white asterisk) with preliminary bone marrow formation (yellow asterisk). Inside, it was observed new vessels formation (black arrows) near to bone surface. 100X. Scale bar = 100 µm. (**c**) At high magnification, bone formed tissue shows pagetoid pattern (white asterisk) with its irregular arrangement. Mature (red) and immature (blue) bone tissue with osteoblasts on surface (black arrow), and osteocytes (white arrow) inside. 400 X magnification. Scale bar = 20 µm. (**d**) Decalcified samples stained by Verhoeff´s elastic stain. Bone defect treated (BDT) shows ossicles (white asterisk) formed around structures like biomaterial debris (gray asterisk). New bone was surrounded by fibroblastic tissue (black asterisk) with many angiogenesis formations containing blue outlined erythrocytes (black arrow). Bone adopted an irregular arrangement resembling pagetoid-like bone (white asterisk). 40X magnification. Scale bar = 100 µm. (**e**) Higher magnification (black square) from 8.d. New pagetoid-like bone (white asterisk) formed on amorphous areas compatible with remains of ELR´s (gray asterisk), surrounded by angiogenesis (black arrow). Osteoblasts (white arrow) and osteocytes (grey arrow) were observed. 400X magnification. Scale bar = 20 µm.

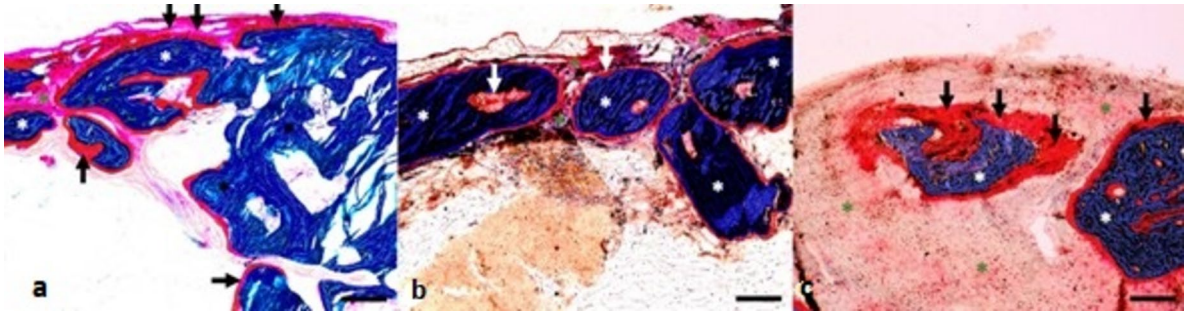


**Figure 9.** Microscopic images from undecalcified samples embedding in methyl methacrylate stained with Masson-Goldner's trichrome. (**a**) In BDUT was observed new bone formation with several islets (white asterisk), immersed in fibroblastic tissue (green asterisk) at control bone defect edge. However, its thickness was minor compared with preexisting bone (black asterisk). Osteoid tissue areas were found (black arrow) on mineralized bone. 40 X. Scale bar = 200 µm. (**b**) At BDT bone formation showed on its edge and central zone, like bone islets (white asterisk) covered by osteoid tissue (white arrow); all surrounded by fibroblastic tissue (green asterisk). 40 X. Scale bar = 200 µm. (**c**) At BDT Bone new formation over BDT central zone surrounded by fibroblastic tissue (green asterisk) and new ossicles (white asterisk) cover by red osteoid thick layer (black arrow). 100 X. Scale bar = 100 µm.

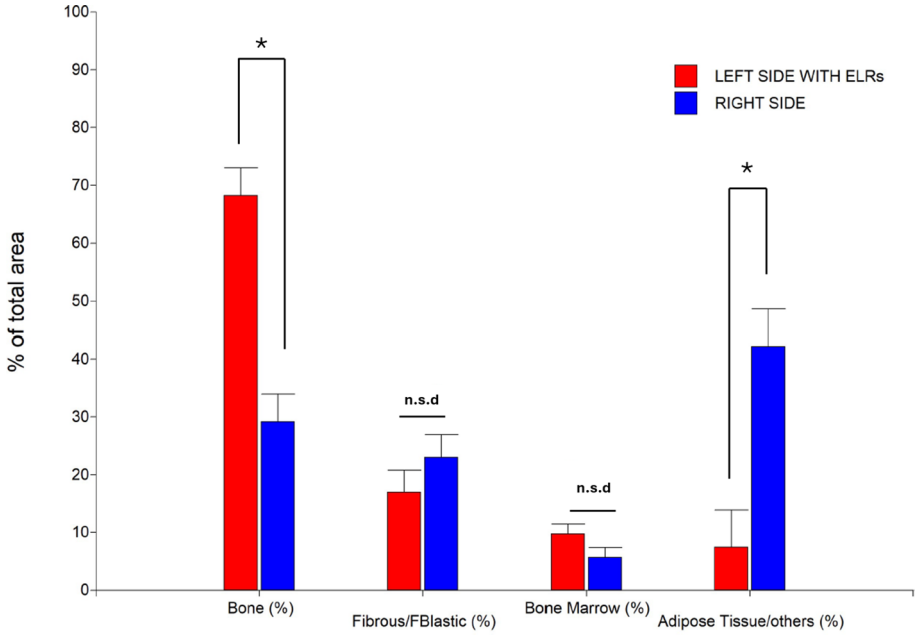


**Figure 10.** An analysis of variance (ANOVA) was conducted for each variable of interest. Subsequently, to detect significant differences, the Tukey test was applied with a significance level of 0.05 (Montgomery, 2013). All assumptions were controlled to ensure confidence in the results (*$p < 0.05$; n.s.d., no significant difference).

## Data availability

The datasets used and/or analysed during the current study available from the corresponding author on reasonable request.

Received: 22 February 2024; Accepted: 7 August 2024
Published online: 30 August 2024

## References

1. Athanasiou, K. A., Zhu, C.-F., Lanctot, D. R., Agrawal, C. M. & Wang, X. Fundamentals of biomechanics in tissue engineering of bone. *Tissue Eng.* **6**, 361–381. https://doi.org/10.1089/107632700418083 (2000).
2. Cointry, G., Capozza, R., Feldman, S. & Reina, P. ¿Los huesos son estructuras genéticas, metabólicas, biomecánicas, o todo a la vez?. *Actual. Osteol.* **5**, 185–195 (2009).
3. Capozza, R. F. *et al.* pQCT-assessed relationships between diaphyseal design and cortical bone mass and density in the tibiae of healthy sedentary and trained men and women. *J. Musculoskelet. Neuronal Interact.* **13**, 195–205 (2013).
4. Mattisson, L., Bojan, A. & Enocson, A. Epidemiology, treatment and mortality of trochanteric and subtrochanteric hip fractures: Data from the Swedish fracture register. *BMC Musculoskelet. Disord.* **19**, 369. https://doi.org/10.1186/s12891-018-2276-3 (2018).
5. Ekegren, C., Edwards, E., de Steiger, R. & Gabbe, B. Incidence, costs and predictors of non-union, delayed union and mal-union following long bone fracture. *IJERPH* **15**, 2845. https://doi.org/10.3390/ijerph15122845 (2018).
6. Johnell, O. & Kanis, J. Epidemiology of osteoporotic fractures. *Osteoporos. Int.* **16**, S3–S7. https://doi.org/10.1007/s00198-004-1702-6 (2005).
7. Camal Ruggieri, I. N., Cícero, A. M., Issa, J. P. M. & Feldman, S. Bone fracture healing: perspectives according to molecular basis. *J. Bone Miner. Metab.* **39**, 311–331. https://doi.org/10.1007/s00774-020-01168-0 (2021).
8. Advances in translational orthopaedic research with speciesspecific multipotent mesenchymal stromal cells derived from the umbilical cord. *Histol Histopathol.* **36**, 19–30 (2021). https://doi.org/10.14670/HH-18-249.
9. Coletta, D. J. *et al.* Synthetic three-dimensional scaffold for application in the regeneration of bone tissue. *JBNB* **09**, 277–289. https://doi.org/10.4236/jbnb.2018.94016 (2018).
10. Xavier, M. *et al.* Biological performance of a bioabsorbable Poly (L-Lactic Acid) produced in polymerization unit: in vivo studies. *F1000Res* **10**, 1275. https://doi.org/10.12688/f1000research.73754.1 (2021).
11. Tang, G. *et al.* Recent trends in the development of bone regenerative biomaterials. *Front. Cell Dev. Biol.* **9**, 665813. https://doi.org/10.3389/fcell.2021.665813 (2021).
12. Venkatesan, A., Fan, J.-Y., Nauman, C. & Price, J. L. A doubletime nuclear localization signal mediates an interaction with bride of doubletime to promote circadian function. *J. Biol. Rhythm.* **30**, 302–317. https://doi.org/10.1177/0748730415588189 (2015).
13. Jahan, K. & Tabrizian, M. Composite biopolymers for bone regeneration enhancement in bony defects. *Biomater. Sci.* **4**, 25–39. https://doi.org/10.1039/C5BM00163C (2016).
14. Saravanan, R. *et al.* Structural basis for endotoxin neutralisation and anti-inflammatory activity of thrombin-derived C-terminal peptides. *Nat. Commun.* **9**, 2762. https://doi.org/10.1038/s41467-018-05242-0 (2018).
15. Kashirina, N. I. & Lakhno, V. D. Correlation effects and configuration of a one-dimensional bipolaron. *Phys. Lett. A* **383**, 126003. https://doi.org/10.1016/j.physleta.2019.126003 (2019).
16. Ranganathan, S. *et al.* Evaluating Shigella flexneri pathogenesis in the human enteroid model. *Infect. Immun.* **87**, e00740-e818. https://doi.org/10.1128/IAI.00740-18 (2019).
17. Zhai, G. *et al.* Serum lysophosphatidylcholines to phosphatidylcholines ratio is associated with symptomatic responders to symptomatic drugs in knee osteoarthritis patients. *Arthritis Res. Ther.* **21**, 224. https://doi.org/10.1186/s13075-019-2006-8 (2019).
18. Athanasiou, K. Sterilization, toxicity, biocompatibility and clinical applications of polylactic acid/ polyglycolic acid copolymers. *Biomaterials* **17**, 93–102. https://doi.org/10.1016/0142-9612(96)85754-1 (1996).
19. Woodruff, M. A. & Hutmacher, D. W. The return of a forgotten polymer—Polycaprolactone in the 21st century. *Prog. Polym. Sci.* **35**, 1217–1256. https://doi.org/10.1016/j.progpolymsci.2010.04.002 (2010).
20. Danhier, F. *et al.* PLGA-based nanoparticles: An overview of biomedical applications. *J. Control. Release* **161**, 505–522. https://doi.org/10.1016/j.jconrel.2012.01.043 (2012).
21. Chen, P. *et al.* Desktop-stereolithography 3D printing of a radially oriented extracellular matrix/mesenchymal stem cell exosome bioink for osteochondral defect regeneration. *Theranostics* **9**, 2439–2459. https://doi.org/10.7150/thno.31017 (2019).
22. Sun, P., Wang, J., Zheng, Y., Fan, Y. & Gu, Z. BMP2/7 heterodimer is a stronger inducer of bone regeneration in peri-implant bone defects model than BMP2 or BMP7 homodimer. *Dent. Mater. J.* **31**, 239–248. https://doi.org/10.4012/dmj.2011-191 (2012).
23. Dinjaski, N. & Kaplan, D. L. Recombinant protein blends: Silk beyond natural design. *Curr. Opin. Biotechnol.* **39**, 1–7. https://doi.org/10.1016/j.copbio.2015.11.002 (2016).
24. An, B. *et al.* The influence of specific binding of collagen–silk chimeras to silk biomaterials on hMSC behavior. *Biomaterials* **34**, 402–412. https://doi.org/10.1016/j.biomaterials.2012.09.085 (2013).
25. Bracalello, A. *et al.* Design and production of a chimeric resilin-, elastin-, and collagen-like engineered polypeptide. *Biomacromolecules* **12**, 2957–2965. https://doi.org/10.1021/bm2005388 (2011).
26. Rodríguez-Cabello, J. C., Martín, L., Alonso, M., Arias, F. J. & Testera, A. M. "Recombinamers" as advanced materials for the post-oil age. *Polymer* **50**, 5159–5169. https://doi.org/10.1016/j.polymer.2009.08.032 (2009).
27. Paulini, M. *et al.* Recombinant proteins-based strategies in bone tissue engineering. *Biomolecules* **12**, 3. https://doi.org/10.3390/biom12010003 (2021).
28. Coletta, D. J. *et al.* <sup/> Bone regeneration mediated by a bioactive and biodegradable extracellular matrix-like hydrogel based on elastin-like recombinamers. *Tissue Eng. Part A* **23**, 1361–1371. https://doi.org/10.1089/ten.tea.2017.0047 (2017).
29. Rodríguez-Cabello, J. C., Girotti, A., Ribeiro, A. & Arias, F. J. Synthesis of genetically engineered protein polymers (recombinamers) as an example of advanced self-assembled smart materials. In *Nanotechnology in Regenerative Medicine* (eds Navarro, M. & Planell, J. A.) 17–38 (Humana Press, 2012). https://doi.org/10.1007/978-1-61779-388-2_2.
30. Ibáñez-Fonseca, A. *et al.* Biocompatibility of two model elastin-like recombinamer-based hydrogels formed through physical or chemical cross-linking for various applications in tissue engineering and regenerative medicine. *J. Tissue Eng. Regen. Med.* https://doi.org/10.1002/term.2562 (2018).
31. Roberts, S. *et al.* Injectable tissue integrating networks from recombinant polypeptides with tunable order. *Nat. Mater.* **17**, 1154–1163. https://doi.org/10.1038/s41563-018-0182-6 (2018).
32. Pescador, D. *et al.* Regeneration of hyaline cartilage promoted by xenogeneic mesenchymal stromal cells embedded within elastin-like recombinamer-based bioactive hydrogels. *J. Mater. Sci. Mater. Med.* **28**, 115. https://doi.org/10.1007/s10856-017-5928-1 (2017).
33. Ibáñez-Fonseca, A. *et al.* Mesenchymal stromal cells combined with elastin-like recombinamers increase angiogenesis in vivo after Hindlimb Ischemia. *Front. Bioeng. Biotechnol.* **10**, 918602. https://doi.org/10.3389/fbioe.2022.918602 (2022).
34. Contessotto, P. *et al.* Elastin-like recombinamers-based hydrogel modulates post-ischemic remodeling in a non-transmural myocardial infarction in sheep. *Sci. Transl. Med.* **13**, eaaz5380. https://doi.org/10.1126/scitranslmed.aaz5380 (2021).

35. Marsico, G. *et al.* Elastin-like hydrogel stimulates angiogenesis in a severe model of critical limb ischemia (CLI): An insight into the glyco-host response. *Biomaterials* **269**, 120641. https://doi.org/10.1016/j.biomaterials.2020.120641 (2021).
36. Meyer, D. E. & Chilkoti, A. Purification of recombinant proteins by fusion with thermally-responsive polypeptides. *Nat. Biotechnol.* **17**, 1112–1115. https://doi.org/10.1038/15100 (1999).
37. Girotti, A. *et al.* Design and bioproduction of a recombinant multi(bio)functional elastin-like protein polymer containing cell adhesion sequences for tissue engineering purposes. *J. Mater. Sci. Mater. Med.* **15**, 479–484. https://doi.org/10.1023/B:JMSM.0000021124.58688.7a (2004).
38. Costa, R. R., Custódio, C. A., Arias, F. J., Rodríguez-Cabello, J. C. & Mano, J. F. Layer-by-layer assembly of chitosan and recombinant biopolymers into biomimetic coatings with multiple stimuli-responsive properties. *Small* **7**, 2640–2649. https://doi.org/10.1002/smll.201100875 (2011).
39. Costa, R. R. *et al.* Stimuli-responsive thin coatings using elastin-like polymers for biomedical applications. *Adv. Funct. Mater.* **19**, 3210–3218. https://doi.org/10.1002/adfm.200900568 (2009).
40. Ruoslahti, E. & Pierschbacher, M. D. Arg-Gly-Asp: A versatile cell recognition signal. *Cell* **44**, 517–518. https://doi.org/10.1016/0092-8674(86)90259-X (1986).
41. Ruoslahti, E. RGD and other recognition sequences for integrins. *Annu. Rev. Cell Dev. Biol.* **12**, 697–715. https://doi.org/10.1146/annurev.cellbio.12.1.697 (1996).
42. Lutolf, M. P. *et al.* Repair of bone defects using synthetic mimetics of collagenous extracellular matrices. *Nat. Biotechnol.* **21**, 513–518. https://doi.org/10.1038/nbt818 (2003).
43. Chung, E. H. *et al.* Biomimetic artificial ECMs stimulate bone regeneration. *J. Biomed. Mater. Res.* **79A**, 815–826. https://doi.org/10.1002/jbm.a.30809 (2006).
44. González de Torre, I. *et al.* Elastin-like recombinamer catalyst-free click gels: Characterization of poroelastic and intrinsic viscoelastic properties. *Acta Biomater.* **10**, 2495–2505. https://doi.org/10.1016/j.actbio.2014.02.006 (2014).
45. Ning, X., Guo, J., Wolfert, M. A. & Boons, G.-J. Visualizing metabolically labeled glycoconjugates of living cells by copper-free and fast Huisgen cycloadditions. *Angew. Chem. Int. Ed.* **47**, 2253–2255. https://doi.org/10.1002/anie.200705456 (2008).
46. García, M. F. M. *et al.* Optimization for bone samples embedded in methyl methacrylate. *J. Hard Tissue Biol.* **31**, 181–186. https://doi.org/10.2485/jhtb.31.181 (2022).
47. Weibel, E. R., Kistler, G. S. & Scherle, W. F. Practical stereological methods for morphometric cytology. *J. Cell Biol.* **30**, 23–38. https://doi.org/10.1083/jcb.30.1.23 (1966).
48. Nosaka, Y. *et al.* Histological an Morphometrical Studies of Bone Formation in rat subcutaneous tissue by BMP-collagen particles. *J. Hard Tissue Biol.* **5**, 188–194 (1996).
49. Wu, Y. *et al.* Role of hydrogels in bone tissue engineering: How properties shape regeneration. *J. Biomed. Nanotechnol.* **16**, 1667–1686. https://doi.org/10.1166/jbn.2020.2997 (2020).
50. Klenke, F. M. *et al.* Impact of pore size on the vascularization and osseointegration of ceramic bone substitutesin vivo. *J. Biomed. Mater. Res.* **85A**, 777–786. https://doi.org/10.1002/jbm.a.31559 (2008).
51. Anada, T. *et al.* Vascularized bone-mimetic hydrogel constructs by 3D bioprinting to promote osteogenesis and angiogenesis. *IJMS* **20**, 1096. https://doi.org/10.3390/ijms20051096 (2019).
52. Choi, Y. H. *et al.* Gelatin-based micro-hydrogel carrying genetically engineered human endothelial cells for neovascularization. *Acta Biomater.* **95**, 285–296. https://doi.org/10.1016/j.actbio.2019.01.057 (2019).
53. DeForest, C. A., Sims, E. A. & Anseth, K. S. Peptide-functionalized click hydrogels with independently tunable mechanics and chemical functionality for 3D cell culture. *Chem. Mater.* **22**, 4783–4790. https://doi.org/10.1021/cm101391y (2010).


## Acknowledgements

The authors are grateful for funding from the Spanish Government ((PID2021-122444OB-100, PID2022-137484OB-I00), Junta de Castilla y León (VA188P23), and Centro en Red de Medicina Regenerativa y Terapia Celular de Castilla y León, Universidad Nacional de Rosario, Argentina, and the advice offered by Dr Professor Paola L. Salvatierra, specialist in statistics, who guided us on methodological aspects and statistical analysis. Sara Feldman is grateful for the support and guidance of Professor Dr Pedro Esbrit, Fundación Jimenez Diaz, Madrid, Spain.

## Author contributions

Camal Ruggieri Iván Nadir: Conceptualization, Data curation, Formal analysis, Investigation, Methodology, Software, Visualization, Writing—original draft, Writing—review and editing. Aimone Mariangeles: Conceptualization, Methodology, Software, Writing—original draft. Juanes-Gusano Diana: Data curation, Investigation, Methodology, Writing—original draft, Writing—review and editing. Ibáñez-Fonseca Arturo: Data curation, Investigation, Methodology, Writing—original draft. Santiago Octavio: Methodology, Writing—original draft. Stur Mariela: Data curation, Formal analysis, Methodology, Resources, Software, Visualization, Writing—original draft. Mardegan Issa João Paulo: Formal analysis, Methodology, Visualization, Writing – original draft. Missana Liliana Raquel: Data curation, Formal analysis, Methodology, Resources, Visualization, Writing—original draft. Alonso Matilde: Data curation, Investigation, Methodology, Writing—original draft. Rodríguez-Cabello José Carlos: Conceptualization, Formal analysis, Methodology, Resources, Supervision, Validation, Visualization, Writing—review and editing. Feldman Sara: Conceptualization, Formal analysis, Investigation, Methodology, Project administration, Resources, Supervision, Validation, Visualization, Writing—original draft, Writing—review and editing.

## Funding

The authors are grateful for funding from the Spanish Government ((PID2021-122444OB-100, PID2022-137484OB-I00), Junta de Castilla y León (VA188P23), and Centro en Red de Medicina Regenerativa y Terapia Celular de Castilla y León and Universidad Nacional de Rosario.

## Competing interests

The authors declare no competing interests.

## Additional information

**Correspondence** and requests for materials should be addressed to I.N.C.R., M.A. or S.F.